



Temperature-dependent AC conductivity and dielectric and impedance properties of ternary In–Te–Se nanocomposite thin films

Pandian Mannu¹ · Matheswaran Palanisamy¹ · Gokul Bangaru¹ · Sathyamoorthy Ramakrishnan¹ · Asokan Kandasami² · Pawan Kumar³

Received: 6 February 2019 / Accepted: 6 June 2019 / Published online: 12 June 2019
© Springer-Verlag GmbH Germany, part of Springer Nature 2019

Abstract

The temperature- and frequency-dependent AC conductivity and dielectric and impedance properties of thermally evaporated ternary In–Te–Se nanocomposite thin films were measured in the temperature range from 100 to 300 K with the frequency range of 20 kHz–2 MHz. The measured dielectric constant (ϵ'), loss tangent ($\tan\delta$), and the ac electrical conductivity (σ_{ac}) values are considerably sensitive to the frequency and temperature. The variations in ϵ' , ϵ'' and $\tan\delta$ characteristics confirm the interfacial polarization. The values of C and ϵ' decrease with frequency, while σ_{ac} increases with both temperature and frequency. The estimated activation energy is found to decrease with increase in temperature. Further, the frequency dependence real (Z') and imaginary parts (Z'') of the impedance spectra of the sample depend on the dielectric relaxation process. The Nyquist plot shows that the radius of the semicircular arc decreases with temperature and reveals a temperature-dependent relaxation process. The mechanism responsible for thermally assisted AC conduction can be due to the electronic hopping of charge carriers.

1 Introduction

Semiconducting chalcogenide materials are the prime candidates for the applications of solid state devices such as photodetectors, phototransistors, optoelectronic, thermoelectric, and phase change memory (PCM) [1–5]. In–Te–Se based ternary system has a number of structural modifications such as α and β phases, and additionally one-third or two-third of In sub-lattices remain vacant in the material. Hence, the presence of stoichiometric phases (In–Se and In–Te) from the phase diagram defines the formation of the In_2Se_3 and In_2Te_3 phases. The presence of defects or impurities at the surface of the material contributes to the interruption of the periodic lattice structure. Consequently, these physical

factors are very important for the density of the localized interface state. The property of localized state varies as a function of temperature, applied bias voltage, and frequency. Hence, the influence of all these parameters results in significant variations in the electrical properties. Though metal chalcogenide-based materials have been extensively studied in the field of microelectronics and thermoelectric applications [5, 6], a great deal of interest has been shown to investigate the dielectric and ac conduction properties of Se–Te based semiconducting glasses by several researchers [7–12]. Dielectric behavior in the solid materials has been reported and explained using various models by Mott et al. [13]. Therefore, the study on dielectric relaxation is an essential topic to understand the origin of loss that has a major role in analyzing the defects in solids [14, 15].

One of the ways to improve the physical properties of chalcogenide is by changing the chemical concentration or by doping metals/semiconducting elements. So that an addition of metal elements including Zn, In, Cd, Ti and Ge into chalcogenides has been performed to improve the electrical transport properties such as AC conductivity and dielectric and impedance properties. Sharma and Kumar have reported the addition of Zn and In into $\text{Se}_{80}\text{Te}_{15}$ glassy alloy and the role of these metals in their physical properties [16].

✉ Matheswaran Palanisamy
mathesphy@gmail.com

¹ Department of Physics, Kongunadu Arts and Science College, Coimbatore, Tamilnadu 641029, India

² Materials Science Division, Inter University Accelerator Centre, New Delhi 110067, India

³ Department of Physics, Government College, Bhiwani, Haryana 127021, India

Additionally, they have investigated Cd- and Ge-dependent AC conductivity and dielectric relaxation properties of the $\text{Se}_{80}\text{Te}_{15}$ alloy compound [17]. Shukla et al. investigated the dielectric property, impedance and AC conductivity of $\text{Se}_{90}\text{Cd}_{10-x}\text{In}_x$ ($x=2, 4, 6$ and 8) glassy alloys and showed a decrease in AC conductivity with the addition of In content due to the decrease in the density of the localized state [9]. The addition of elements such as Ag, Cd, In, Sb and Zn into binary $\text{Se}_{100-x}\text{Te}_x$ alloys modifies the physical properties of the particular composition [18–21]. The enhancement in AC conduction with an addition of Cd, In and Sb on $\text{Se}_{80}\text{Te}_{20}$ alloy was performed by changing the Te element [19, 20]. Based on the dielectric relaxation properties of Ag-, Zn- and Cd-doped $\text{Se}_{70}\text{Te}_{28}$ system, Dohare et al. showed the dominance of bipolaron hopping over the potential barrier [10].

In general, undoped chalcogenides exhibit poor electrical conductivity. Additions of metals such as Zn, In, Cd, Ti and Ge into chalcogenides has been largely carried out to improve their electrical transport properties. The incorporation of impurity element acts as a chemical modifier and also produces compositional disorder in the material and leads to change in the electrical property of chalcogenides [22]. From the above reported studies, it is clear that the addition of a third element (metal basis) to chalcogenide alloys significantly modifies the electrical properties of the materials. Adding Se in InTe enhances the AC conductivity and impedance properties as a function of frequency and temperature. These investigations also help to understand the conduction mechanisms in these materials. Literature survey suggests that limited reports are available on the physical properties of $\text{In}_2(\text{Te}_{1-x}\text{Se}_x)_3$ nanocomposites.

The addition of Se $\text{In}_2(\text{Se}_x\text{Te}_{1-x})_3$ system in the present work also shows higher dielectric constant value in comparison to that of the earlier reported binary $\text{Se}_{70}\text{Te}_{30}$ and $\text{Se}_{0.85}\text{Te}_{0.15}$ system, and hence reveals the effect of third elements to the chalcogenides which improves the dielectric properties considerably.

The electrical conductivity of the In_2Te_3 phase is greater than that of the In_2Se_3 phase. To tune the electrical properties one can mix these two phases and obtain ternary In–Se–Te nanocomposite thin films that possess variable physical properties. Recently, it has been reported that these two binary In_2Te_3 and In_2Se_3 phases exhibit good electrical and thermal properties [23]. It is observed that the as-deposited films crystallize at the annealing temperature of 250°C with promising thermoelectric properties and higher thermal stability of the materials. Further, in the In–Se and In–Te phase diagrams, both these phases can mix at different stoichiometric compositions and exhibit different physical properties. In this ternary phase, the compositions of In—40%:Te—54%:Se—6% were studied earlier and reported that they exhibit very good resistive switching and thermoelectric properties [23, 24]. Hence, this composition has

been selected to study the dielectric and AC conductivity properties.

In the earlier investigation, In_2Te_3 bilayer thin films were prepared by sequential thermal evaporation [25]. In that case, the variations in capacitance and dielectric constants were measured in the low-frequency range (100 Hz–60 kHz) and above room temperature range (291–448 K). The present work reports the dielectric properties of Cu/InTeSe/Cu structures, especially in the low-temperature range (100–300 K) and high-frequency ranges of 20 kHz–2 MHz. The present work aims to explore the addition of a third element Se into the In–Te metal chalcogenides and study its AC conductivity and impedance properties in the wide frequency range from 20 kHz to 2 MHz. Limited studies have been reported on the dielectric properties of In–Te–Se nanocomposites-based thin films and this is the first report to the best of our knowledge on ternary In–Te–Se nanocomposites system. Here, we report the dielectric, impedance spectra with related parameters as a function of frequency/temperature for the InTeSe dielectric layer. Moreover, the dielectric parameters ϵ' , $\tan\delta$, and σ_{ac} were determined and analyzed from the measured value of capacitance.

2 Experimental methods

The elements In, Te and Se (5 N—purity) in the desired composition (In—40%:Te—54%:Se—6%) were taken to prepare ternary In–Te–Se nanocomposite thin films. The powder form of this composition was taken in a quartz tube and quartz ampoules were fused at a reduced 1×10^{-5} mbar pressure; subsequently, the sealed quartz tube was annealed at 900°C for 12 h using a rotating furnace. The temperature of the furnace was raised slowly at a rate of $4\text{--}5^\circ\text{C}$ per min throughout the experiment. During the heating processes, melted ampoules were constantly rocked by rotating the ceramic rod to form homogeneous stoichiometric alloys. The molten state of the sample was quenched to room temperature to form the stoichiometric compound. The quenched materials were taken out by breaking the quartz tube. The ingots were mixed and ground to make a fine powder for film deposition. Primarily, a Cu bottom electrode (5 N purity) of thickness 200 nm was deposited on the cleaned glass substrates by the thermal evaporation technique at a reduced pressure of 2×10^{-6} mbar in Ar atmosphere using suitable masks. The prepared In–Te–Se nanocomposites were deposited as a dielectric layer (500 nm thickness), followed by the deposition of a top electrode (Cu) to form metal–semiconductor–metal (MSM) structure. Both the electrode and dielectric layers' thickness was monitored by quartz crystal thickness monitor. The rate of deposition for both layers was maintained at $\approx 10 \text{ \AA/s}$ and the substrate temperature was also maintained at room temperature ($\sim 27^\circ\text{C}$) throughout

the deposition. Figure 1 shows the molten state of the materials and fabricated Cu/InTeSe/Cu film structure for the present study.

The structural properties were studied by X-ray diffraction (XRD) using the Shimadzu 6000 facility. The surface morphology of the samples was characterized by field emission scanning electron microscopy (FESEM) along with energy-dispersive X-ray analysis using the CARLZEISS SIGMA version with the Quantax 200-Z10 EDS detector. The interactive PB-ZAF was chosen by default. Quanta optimization was done using a standard cobalt sample 99.995% (metal basis). Atomic force microscopy (AFM) image was recorded by tapping mode using Nanoscope IIIa model. Transmission electron microscopy (HRTEM) image of the sample was also analyzed by the JEOL JEM 2100 model. Dielectric and impedance spectrum measurements were carried using Agilent E-4980A LCR meter, attached to a Lakeshore 325 temperature controller, interfaced via the LabView program in the temperature range from 100 to 300 K with the frequency range of 20 kHz–2 MHz.

3 Results and discussion

3.1 Structural analysis

Figure 2 represents the measured diffraction pattern of In–Te–Se nanocomposites thin films. The dominant peaks at 23.10° and 40.35° correspond to (21 $\bar{5}$), (21 $\bar{1}$ $\bar{4}$) planes of $\text{In}_2(\text{SeTe})_3$ phase (JCPDS: 23-0294). In addition, the high-intensity peaks at 67.12° and 77.25° correspond to the (12 4 4), (11 9 5) plane of the In_2Te_3 phase (JCPDS: 71-0250). The low-intensity peaks at 27.68°, 47.10° and 63.80° correspond to the (0 0 6), (2 0 8), (8 8 6) plane of the In_2Se_3 , In_2Se_3 and In_2Te_3 phases (JCPDS: 33-1488, 71-0250). The deposited $\text{In}_2(\text{Te}_{1-x}\text{Se}_x)_3$ thin films were annealed at 250 °C under an argon atmosphere for 30 min. It is evident that annealing treatment on these materials shows variation in the peak intensity only as it exhibits the same diffraction peak

Fig. 1 The molten state of the materials and the fabricated Cu/InTeSe/Cu film structure

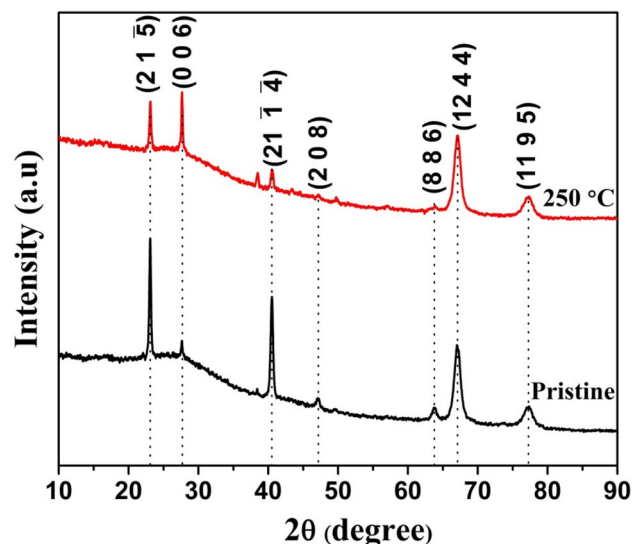
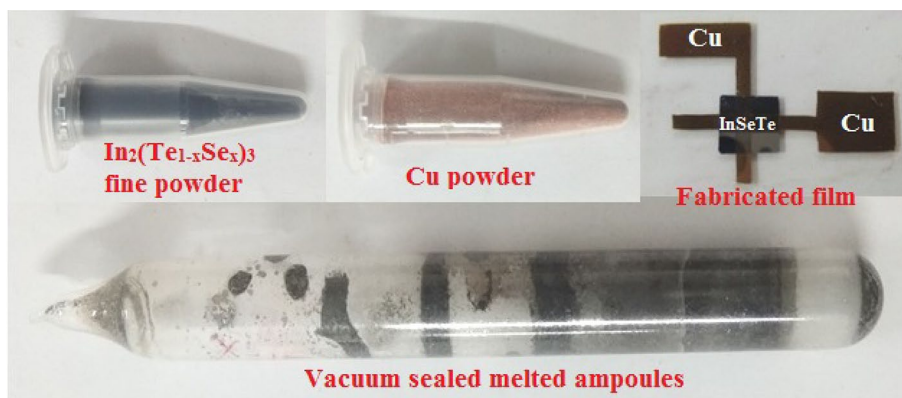


Fig. 2 XRD pattern of the In–Te–Se nanocomposites thin film

in comparison to the as-deposited film and no peak shift is observed (shown in Fig. 2). The decreased peak intensity confirms the improvement in the crystallinity of the annealed sample. The deposited films crystallize at 250 °C and show good thermal stability. The crystallite size was calculated using the following Scherer's formula,

$$D = k\lambda/\beta \cdot \cos \theta, \quad (1)$$

where the constant ' k ' is the shape factor (0.94), ' λ ' is the wavelength of X-rays (1.54 Å for Cu $K\alpha$), ' θ ' is the Bragg's angle and ' β ' is the full width at half maximum of diffraction peak measured in radians. The average crystallite size (D) was estimated from the dominant peaks and is found to be 40.72 nm. The average crystallite size is found to be 45.57 nm for films annealed at 250 °C. It is concluded that thermal annealing leads to increase in the crystallite size as compared to as-deposited films. The experimentally observed peak positions and $d_{(hkl)}$ values matched with the standard JCPDS values, and structural parameters of pristine

and thin film samples of In–Te–Se nanocomposites annealed at 250 °C are presented in Table 1.

3.2 Morphology and compositional analysis

Figure 3a shows the FESEM image of as-deposited In–Te–Se nanocomposite thin film. It clearly confirms that the prepared samples have a homogeneous surface with spherically shaped grains. From Fig. 3b, the annealed 250 °C sample clearly shows agglomeration of the grains and the formed grains are bigger in size in comparison to the as-deposited sample. This may arise due to the agglomeration of smaller

grains leads to the formation of bigger grains, which is consistent with XRD studies (i.e., where the crystallite size increases). Larger spherical geometry of the grains in the annealed sample reveals the reduced grain boundaries. The presence of dense grain boundaries could improve the grain and grain boundary effect in $\text{In}_2(\text{Te}_{1-x}\text{Se}_x)_3$ thin film. In addition to that, the dielectric properties of materials mostly depend on the grain boundaries, because applied electric field to the system produces a space charge polarization in the grain boundaries. Therefore, high dielectric constant at the low-frequency region can be attributed to the presence of larger grain boundaries in the present work. At higher

Table 1 Structural parameters of pristine and In–Te–Se nanocomposite thin film annealed 250 °C

Sample InSeTe	2θ (degree)	Phase and orientation (hkl)	Obs. d_{hkl} (Å)	Cal. d_{hkl} (Å)	Average crystalline size (nm)
Pristine	23.10	$\text{In}_2(\text{Se Te})_3$ (21 $\bar{5}$)	3.81	3.86	40.72
	27.68	In_2Se_3 (0 0 6)	3.22	3.28	
	40.35	$\text{In}_2(\text{Se Te})_3$ (21 $\bar{1}$ $\bar{4}$)	2.22	2.17	
	47.10	In_2Se_3 (2 0 8)	1.90	1.97	
	63.80	In_2Te_3 (8 8 6)	1.44	1.37	
	67.12	In_2Te_3 (12 4 4)	3.20	3.25	
	77.25	$\text{In}_2(\text{Se Te})_3$ (11 $\bar{9}$ $\bar{5}$)	1.23	2.26	
Annealed 250 °C	23.21	$\text{In}_2(\text{Se Te})_3$ (21 $\bar{5}$)	3.81	3.84	45.57
	27.75	In_2Se_3 (0 0 6)	3.22	3.26	
	40.43	$\text{In}_2(\text{Se Te})_3$ (21 $\bar{1}$ $\bar{4}$)	2.22	2.15	
	47.16	In_2Se_3 (2 0 8)	1.90	1.95	
	63.87	In_2Te_3 (8 8 6)	1.44	1.35	
	67.16	In_2Te_3 (12 4 4)	3.20	3.25	
	77.36	$\text{In}_2(\text{Se Te})_3$ (11 $\bar{9}$ $\bar{5}$)	1.23	2.27	

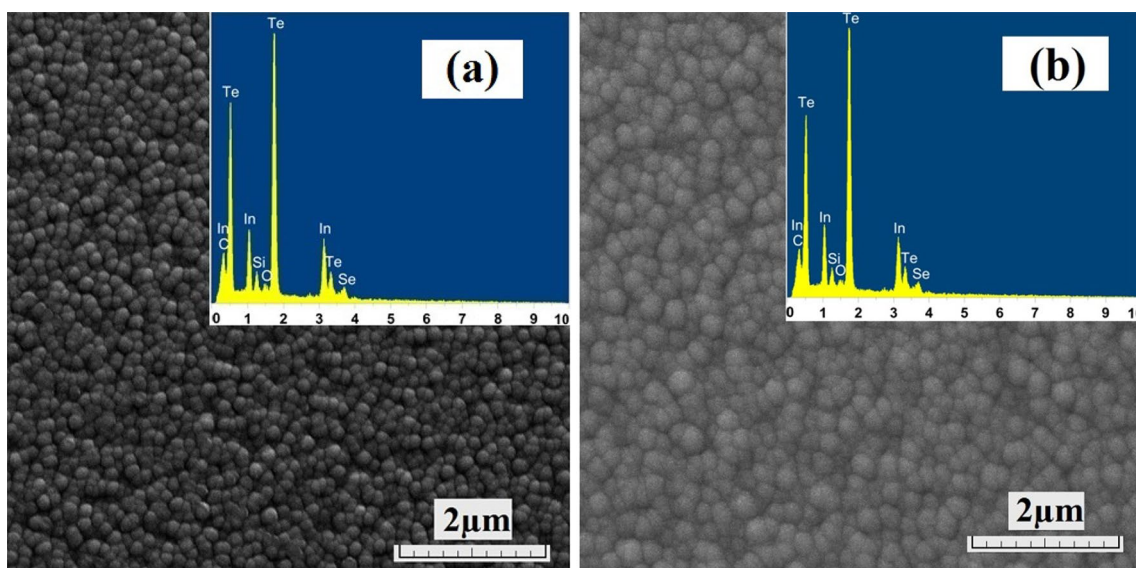


Fig. 3 FESEM image and EDS spectrum of pristine (a) and annealed 250 °C (b) In–Te–Se nanocomposites thin film

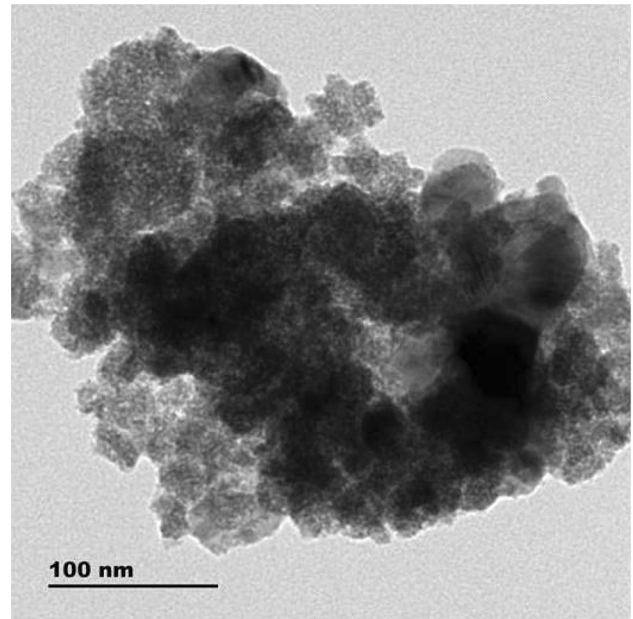
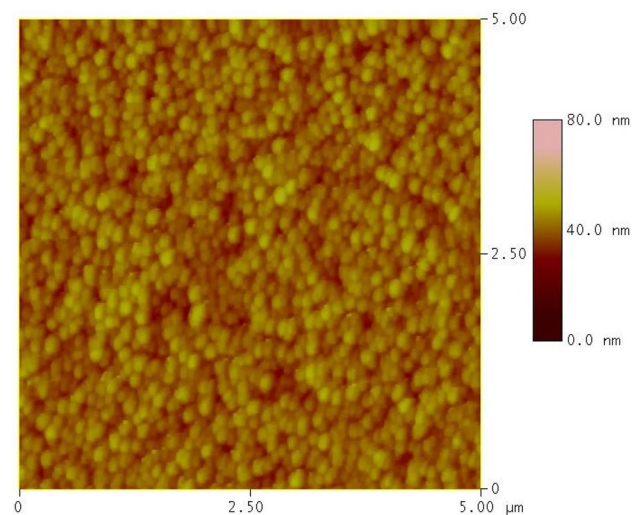
Table 2 Elemental composition of In–Te–Se nanocomposite thin film

Sample InSeTe	Actual composition (%)			Composition based on EDS results (%)			Elements from the glass substrate		
	In	Te	Se	In	Te	Se	C	O	Si
Pristine	40	54	6	30.44	51.27	5.28	4.36	1.89	6.76
Annealed 250 °C	40	54	6	30.30	51.65	5.34	4.36	1.70	6.65

frequency, the grains are limited to having a small dielectric constant. Table 2 shows the elemental composition of as-deposited and annealed 250 °C In–Te–Se nanocomposite thin films. The EDS spectrum confirms the presence of In, Se and Te materials. Additionally, elements silicon, carbon and oxygen have been observed, which are normally present in the glass substrate. The EDS data of pristine sample show the compositions as 30.44%:51.27%:5.28%. There is a deviation from the initial compositions mainly in In due to the thermal evaporation processes used wherein vaporization occurs. The as-grown composition remains similar even after thermal annealing and matches with that of as-prepared ingots as shown in Table 2.

The actual elemental ratios for In:Te:Se are 40%:54%:6%. However, the elemental ratio is found to differ as evident from the EDS analysis. The deviation is explained as follows: the pure crystalline/amorphous In_2Se_3 phase was observed for the higher concentration of Se. From the calculated and measured elemental compositions, Te and Se elemental ratio shows smaller deficiency compared to In. It is also evident that because of the bonding energy difference, the formation of the InSe phase is more in comparison to the InTe phases. Additionally, In ions are known to get evaporated or vaporized significantly during the thermal evaporation processes, leading to a deficiency of its percentage. Additional elements Si, O and C arise from the glass substrate. These elements do not contribute to the physical properties of In–Se–Te. Moreover, the percentage seen in the EDS spectrum is too small. Therefore, AC conductivity and dielectric properties are mainly from the In–Se–Te system.

The TEM image of the as-deposited sample was recorded by taking out the material layer (In–Te–Se) from the top of the glass substrate. The TEM image of the In–Te–Se nanocomposite thin film revealed that the spherical-sized particles agglomerated with each other with tiny pores (shown in Fig. 4). The 2D AFM micrograph image of as-deposited In–Te–Se nanocomposite film was obtained and is shown in Fig. 5. The spherical-shaped grains are similar to the FESEM images. The average grain size was estimated from the AFM image and found to be ~ 45 nm. The calculated values of average surface roughness (R_a) and the root mean square (RMS) R_q were found to be ~ 4.83 and ~ 5.96 nm, respectively. The FESEM and AFM and TEM images exhibit a very similar surface morphology with spherical-shaped

**Fig. 4** TEM image of pristine In–Te–Se nanocomposite thin film**Fig. 5** AFM image of pristine In–Te–Se nanocomposite thin film

grains/spherical-shaped particles on the entire surface. The estimated average crystallite size determined by XRD was found to be 40.72 nm, and the average grain size \sim 37.24 nm was estimated from the FESEM/TEM with similar result evident in the AFM image.

3.3 Dielectric properties

Figure 6a, b represents the temperature and frequency dependence capacitance of In–Te–Se Se nanocomposite thin film. The capacitance values are found to be higher in the low-frequency region and then gradually decreases with an applied frequency. The distribution of interfacial charge carriers is an important factor for the enhancement of capacitance value at the frequency region [26]. The accumulation of additional charge carriers at the interface states led to excess capacitance at higher temperature, which was found to increase with temperature as shown in Fig. 6b [27]. Blocking of charge carriers at the electrode could be the reason for the high value of capacitance at

the low-frequency region. At the low temperature region (below 200 K), the rate of increase in capacitance value is lower than that in the high temperature region (above 200 K) as shown in Fig. 6c. On the other hand, the capacitance value gradually decreases at constant temperature with increase in the applied frequency. The characteristics of the capacitance of $\text{In}_2(\text{Te}_{1-x}\text{Se}_x)_3$ thin film reveals the semiconducting nature of materials [27, 28]. The observed results are highly consistent with the earlier reports in semiconducting thin films [28, 29]. Padma et al. reported that the capacitance was weakly dependent on the frequency at low temperature and strongly dependent at higher temperature in Ir/InGaN schottky structure [28]. Further, the capacitance value decreases significantly with increase in frequency. They have also shown that the capacitance values are dominated by the depletion capacitance of the Schottky diode that is bias dependent and frequency independent. Ridge et al. [29] investigated the amorphous Pb–Ti–O thin film capacitors and showed rapid increase in the capacitance with decrease in the frequency

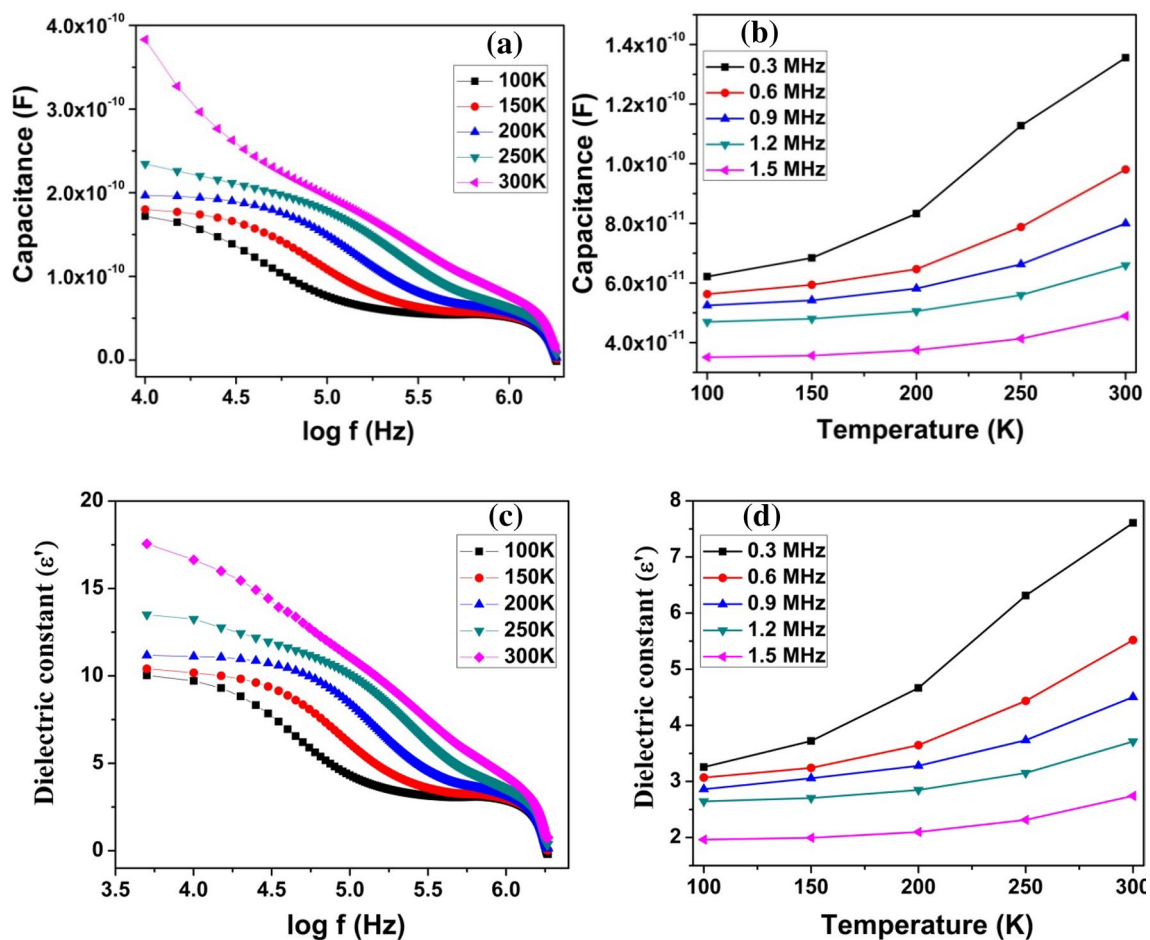


Fig. 6 Capacitance characteristics as a function of frequency (a) and temperature (b). Dielectric constant behavior with frequency (c) and temperature (d)

range. The reason for the dominant increase in capacitance is explained by model of charge carriers blocked at the electrodes. Additionally, the formed space charge layer also leads to a large increase in capacitance value.

The dielectric constant (ϵ') is measured by using the following relation,

$$\epsilon' = \frac{Cd}{\epsilon_0 A}, \quad (2)$$

where capacitances is shown by (C), thickness by (d), free space permittivity by (ϵ_0), and area of the dielectric layer by (A).

The loss tangent is represented by the relation below,

$$\tan \delta = \frac{\epsilon''}{\epsilon'}, \quad (3)$$

where δ is the phase difference of applied field to that of induced current.

Figure 6c, d represents the dielectric constant as a function of frequency and temperature. The observed ϵ' value is higher at low frequency and decreases with increase in frequency. Similarly, Fig. 6d depicts higher value of ϵ' at low frequency in the higher temperature region. The high value of ϵ' at the low-frequency region can be explained on the basis of the Maxwell–Wagner model [30]. Koop's theory [31] assumes that the solids are formed of fine-conducting grains separated as grain boundaries and high resistive thin layers. Thus, an applied electric field to the system produces a space charge polarization in the grain boundaries. The term space charge polarization mostly depends on the availability of free charge carriers and conductivity of the samples. High dielectric constant value at the low-frequency region can be attributed to the grain boundaries. At higher-frequency region, the grains are limited to having a small dielectric constant and, therefore, the grain boundary is an important factor for the dielectric behavior in the solid materials. The measured results agree with the Debye relaxation model for orientational polarization [32]. The deviation in the dielectric constant with the temperature is related to the charge carriers. At low temperature, some of the charge carriers tend to orient themselves with respect to the direction of the applied field; hence, they possess a weak contribution of charge carriers to the polarization, leading to low dielectric constant value. On the other side, more charge carriers get sufficient thermal excitation energy at higher temperature; therefore, they respond to the change in the external field easily. This enhances the polarization of charge carriers, leading to an increase in ϵ' [32]. The obtained results are consistent with those of the earlier reported thin film materials [33, 34].

Addition of metal elements (Zn, Sn, Ag, Cd and In) into Se–Te based chalcogenide improves the dielectric

properties. Dohare et al. [10] have shown that the addition of Ag, Zn and Cd to the $\text{Se}_{70}\text{Te}_{30}$ system improved the dielectric constant value and the estimated values are about ~ 45 to 85 in comparison to binary $\text{Se}_{70}\text{Te}_{30}$ value ~ 9 at 303 K. Sharma et al. [16] reported the dielectric value of about ~ 7 for $\text{Se}_{0.85}\text{Te}_{0.15}$ glassy alloy at 300 K, which was further enhanced to ~ 17 and ~ 37 for the $\text{Se}_{0.75}\text{Te}_{0.15}\text{In}_{0.10}$ and $\text{Se}_{0.75}\text{Te}_{0.15}\text{Zn}_{0.10}$ ternary system, respectively.

The addition of Pb_x ($x=6$) to ternary $\text{Te}_{20}\text{Sn}_2\text{Se}_{78-x}$ system also improved the dielectric constant value by about ~ 90 and it was found to be higher than the $\text{Te}_{20}\text{Sn}_2\text{Se}_{78}$ sample value of ~ 13 at 303 K [8]. The present $\text{In}_2(\text{Se}_x\text{Te}_{1-x})_3$ system also shows similar behavior and is consistent with the above investigations. Moreover, the addition of metal elements to the chalcogenides improved the dielectric performance of the materials. Hence, the addition of In₂ to $(\text{Se}_x\text{Te}_{1-x})_3$ system in the present work also shows a higher dielectric constant value in comparison to that of earlier reported binary $\text{Se}_{70}\text{Te}_{30}$ and $\text{Se}_{0.85}\text{Te}_{0.15}$ systems that reveals the addition of a third element to the chalcogenides enhances the dielectric properties. Figure 7a shows the frequency dependence of dielectric loss at different temperatures. The plot reveals that the loss factor decreases with increasing frequency. The loss factor has a large value at the low-frequency range and is consistent with the earlier reports [35, 36]. The energy loss is high at the low-frequency region, as it requires more energy for the hopping of charge carriers in between the energy levels. On the other hand, the high-frequency region promotes the electron movement between the energy levels. Hence, the energy loss is small at the high-frequency region.

Here, the comparisons of electrical parameters between the In_2Te_3 bilayer film [25] and $\text{In}_2(\text{Te}_{1-x}\text{Se}_x)_3$ films are given in Table 3. It is observed that the $\text{In}_2(\text{Te}_{1-x}\text{Se}_x)_3$ thin film exhibits higher capacitance and dielectric values in comparison to that reported for the In_2Te_3 system, especially in the low temperature region (100 – 300 K). Moreover, larger dielectric constant value ~ 17 at 300 K is achieved in the present ternary $\text{In}_2(\text{Te}_{1-x}\text{Se}_x)_3$ system compared to the reported binary $\text{Se}_{70}\text{Te}_{30}$ value ~ 9 at 303 K. Therefore, the addition of a third element significantly improves the electrical properties and could provide great scope for electronic devices.

The temperature dependence $\tan\delta$ for different frequencies is shown in Fig. 7b. At selected frequencies, the $\tan\delta$ value is found to increase as a function of temperature. This mechanism can be incorporated with lagging behind of charged ion species with the applied energy that leads to polarization. According to Stevels et al. [37], the relaxation mechanism can be governed by: conduction loss, dipole loss and vibrational loss. At low temperature, the conduction loss has minimum value which is proportional to σ_{ac} conductivity. An increase in the conduction loss with temperature can be due to the increase in σ_{ac} conductivity, resulting increase in the dielectric loss as a function of temperature. The other

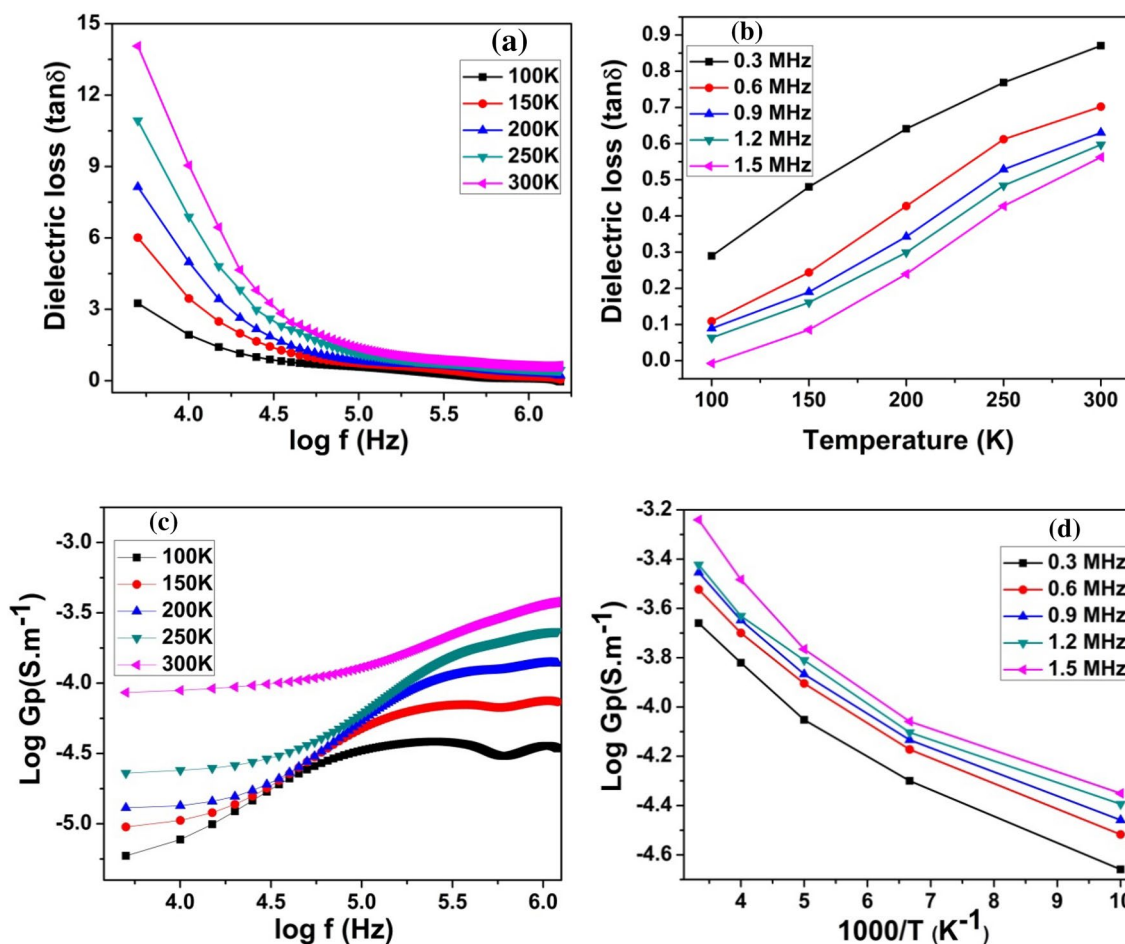


Fig. 7 Dielectric loss as a function of frequency (a) and temperature (b). AC conduction behavior with frequency (c) and temperature (d)

Table 3 Comparison of electrical parameters

Electrical parameters for In ₂ Te ₃ system		Electrical parameters for In ₂ (Te _{1-x} Se _x) ₃ system			
Capacitance (nF) at 10 kHz	448 K	~20	Capacitance (F) at 0.3 MHz		
	398 K	~17	300 K	~3.9	
	348 K	~16	250 K	~2.4	
	291 K	~14	200 K	~2.0	
Dielectric constant (ε') at 10 kHz	448 K	~2.6	100 K	~1.8	
	398 K	~2.3	Dielectric constant (ε') at 0.3 MHz	300 K	~17
	348 K	~2.0	250 K	~14	
	291 K	~1.8	200 K	~12	
			100 K	~10	

two losses involve (i) migration of ions and (ii) contribution of ions jumping over the highest barrier. At low frequency (below 50 kHz), the factors include ion migration, contribution of ions jump, and ions polarization loss leading to variation in tanδ value. The tanδ value is found to be minimum below the 50 kHz region; therefore, ion vibration could be the only source of dielectric loss that produces minimum value. Moreover, both conduction and vibration loss has minimum value at low temperature. However, the increase

in temperature enhances the hopping of charge carriers. This conduction is attributed to hopping of charge carriers from one localized charge state to another state, which results in conduction loss [38]. Furthermore, the vibration loss also increases with rise in temperature. Moreover, AC and dielectric properties of In₂(Te_{1-x}Se_x)₃ thin film were studied especially at the low temperature range (100–300 K). A larger dielectric constant value ~ 17 at 300 K was achieved in the present ternary In₂(Te_{1-x}Se_x)₃ system compared to the

reported binary $\text{Se}_{70}\text{Te}_{30}$ value ~ 9 at 303 K. The addition of a third element (Indium) improves the dielectric properties of $\text{In}_2(\text{Te}_{1-x}\text{Se}_x)_3$ thin film.

3.4 AC conduction studies

AC conductance (Gp) can be calculated from the measured dielectric parameters by the following relation,

$$\sigma_{ac} = \omega \epsilon_0 \epsilon_r \tan \delta, \quad (4)$$

where $\epsilon_r = C/C_0$ is the relative permittivity, C_0 is the capacitance in vacuum, and $\tan \delta$ is the loss factor. Figure 7c represents AC conductivity of the present system as a function of frequency at different temperatures. σ_{ac} vs. frequency plot exhibits two different conduction processes at the low and intermediate temperature. In general, the frequency-dependent AC conductivity in these types of materials can be explained by the following relation [39],

$$\sigma_{ac} = Af^n, \quad (5)$$

where A is temperature-dependent constant and n is found to be the frequency exponent parameter. It is evident from Fig. 7c that σ_{ac} conductivity increases linearly with an increase in the frequency. The frequency-dependent exponent ' n ' values are estimated by plotting straight line slope from these figures and the values ranging from 0.51 to 1.37, which shows decreasing characteristics with temperature. The obtained results agree with the those of earlier investigation on semiconducting thin film [37]. At below ~ 50 kHz frequency region, conductivity increases linearly with frequency. In this region, the value for ' n ' is found to be 0.51, confirming the conduction mechanism corresponding to the translational hopping [39], i.e., $0 < n < 1$. At above 50 kHz, the plot exhibits similar trends to frequency-dependent conductivity. In this region, the n value is found to be 1.37, i.e., $1 < n < 2$, showing that the conduction mechanism is due to the well localized hopping or reorientational motion [39]. It is evident that σ_{ac} conductivity increases as a function of both temperature and frequency, and such a behavior reveals the semiconducting nature of the $\text{In}_2(\text{Te}_{1-x}\text{Se}_x)_3$ film. The frequency exponent ' n ' has temperature dependence and it decreases with increase in temperature. Therefore, the frequency dependence of $\text{In}_2(\text{Te}_{1-x}\text{Se}_x)_3$ film reveals that the mechanism responsible for thermally assisted AC conduction can be due to electronic hopping. To explain the σ_{ac} conductivity as a function of both temperature and frequency, various theoretical models have been explored to correlate with $n(T, \omega)$. Most of the theories on semiconducting materials assumed that carrier motion occurs through quantum mechanical tunneling (QMT) between localized (defect) states near the Fermi level [40, 41]. Here, ' n ' is the frequency dependence but temperature independence and it has a value of 0.783 for the QMT model [40]. Therefore, the

temperature dependence of ' n ' can be met in the tunneling models if the carrier forms a small or large polaron.

From Fig. 7c σ_{ac} versus frequency plot, nearly all the curves are approximate to the power law dependence of ac conduction for the present system. It is correlated to short range hopping of charge carriers tunneling from a localized energy barrier of different heights. Individually, the potential pair has a definite time constant for the transition of one energy barrier to another. Generally, higher energy barrier may take larger time constant for the transition than the smaller energy barrier. Therefore, the traps with high activation energy can respond consistently at low frequency. Nonadiabatic hopping of the carriers defines the conductivity nature at the low-frequency region for the present system. Hence, the values of n lie from 0.5 to 1.0, confirming the hopping of charge carriers between a random distribution of localized charge states. Single and multiple hopping occurrences in the materials are correlated to the high and low ' n ' values, respectively. Therefore, the mechanism responsible for AC conduction is electronic hopping of charge carriers [29]. The values of AC conductance (Gp) value for In–Te–Se nanocomposites are presented in Table 4. The behavior of AC conductance and Gp values are consistent with the earlier investigations on several materials [38, 42].

Figure 7d represents the plot of $\log(\text{Gp})$ vs. $1000/T$ at different frequency ranges. The plot clearly confirms that σ_{ac} increases linearly with frequency and temperature. Generally, the temperature-dependent Arrhenius nature has been observed in various physical and chemical parameters [43–45]. The estimated activation energy is found to decrease from 0.097 to 0.042 eV with temperature (100 K and 300 K respectively for 0.3 MHz). Similar trends also have been observed at higher frequency (1.5 MHz), showing that the activation energy decreases from 0.086 to 0.035 eV.

Table 4 The values of AC conductance (Gp) for In–Te–Se nanocomposites

Temperature (K)	Frequency (MHz)	AC conductance (Gp) (S m^{-1})
100	0.5	4.81×10^{-05}
	1.0	3.97×10^{-05}
	1.5	3.58×10^{-05}
	2.0	2.30×10^{-05}
200	0.5	1.22×10^{-05}
	1.0	5.38×10^{-04}
	1.5	4.72×10^{-04}
	2.0	3.91×10^{-04}
300	0.5	3.77×10^{-04}
	1.0	3.43×10^{-04}
	1.5	3.05×10^{-04}
	2.0	2.45×10^{-04}

Low activation energy implies the conduction mechanism in this film, revealing hopping of charge carriers and corroborates with the earlier reports [46, 47]. Moreover, the activation energy is found to reduce with increase in frequency attributed to the increased charge carriers between the localized states with an applied frequency. Moreover, activation energy decreases and AC conductance increases with increase in applied frequency. Similar results also have been reported on other chalcogenide materials [48].

3.5 Impedance analysis

Figure 8a, b represents the frequency dependence of real (Z') and imaginary (Z'') part of the InTeSe film at different temperatures. Figure 8a clearly shows that Z' decreases as a function of temperature which indicates negative temperature coefficient of the resistance in the system [49]. At a certain frequency region (below 0.3 MHz), the Z' value decreases significantly, whereas it remains almost constant at the higher-frequency region (above 0.3 MHz).

Figure 8b shows the Z'' versus frequency plots at different temperatures, revealing the peak position shift toward the higher-frequency region. The increase in the applied frequency leads to shifts in the peak position to the higher-frequency region and also reduces the intensity of the peak position with rise in temperature as well. These results suggest the spread of relaxation time and the temperature-dependent electrical relaxation mechanism in the material. Additionally, occurrence of defects/vacancies or immobile species/electrons in the material determines the relaxation process in these materials.

From the relaxation system, the relaxation time (τ) can be obtained from the position of loss peak value in the Z'' at different frequency plots using the relation: $\tau = 1/\omega$. Figure 8d represents $\ln \tau$ versus reciprocal temperature $1000/T$ of the present InTeSe system. It clearly shows the temperature-dependent relaxation time in the materials. The experimental data can be evaluated by Arrhenius expression as follows,

$$\tau = \tau_0 \exp(\Delta E_a/k_b T), \quad (6)$$

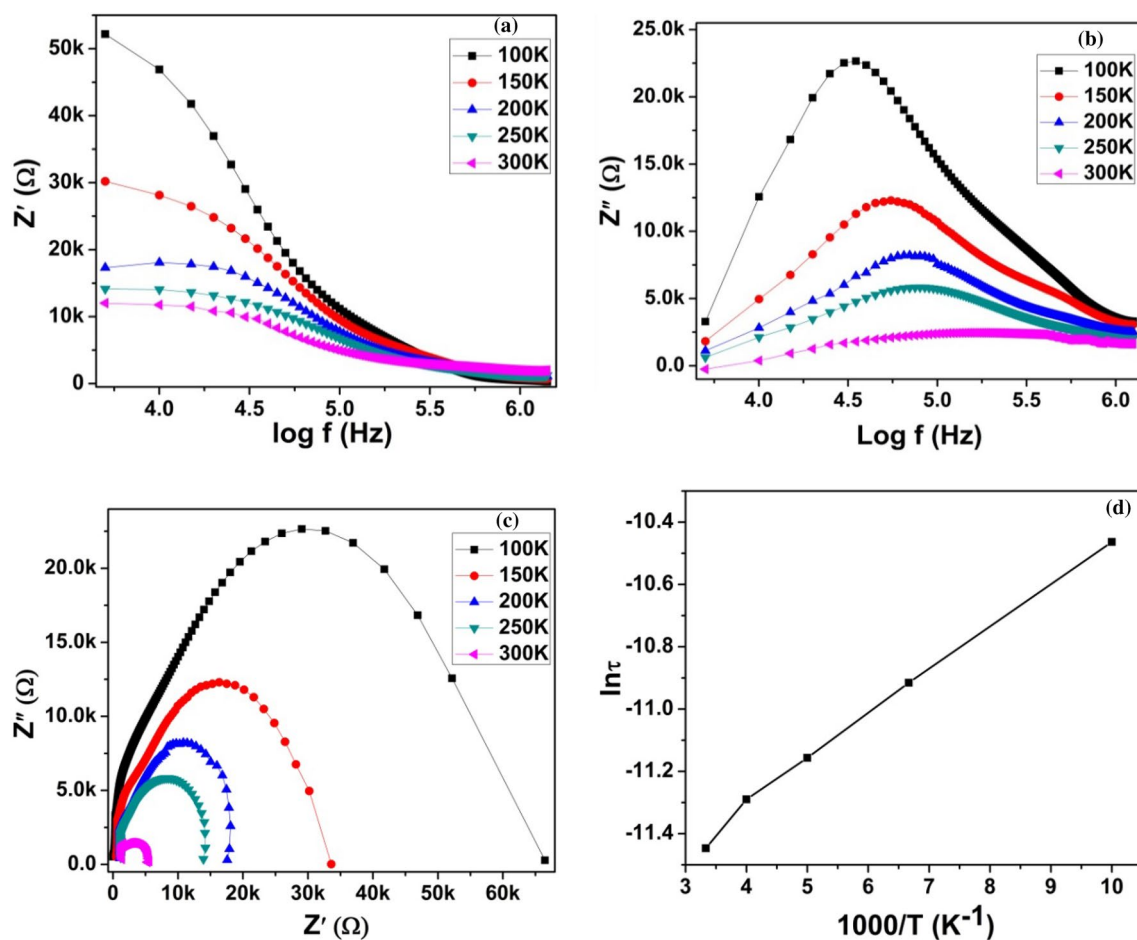


Fig. 8 Frequency dependence of **a** real part, Z' , **b** imaginary part, Z'' , **c** Nyquist plot of complex impedance spectrum of In₂(Te_{1-x}Se_x)₃ thin film at different temperatures and **d** plot of $\ln \tau$ versus $1000/T$

where E_a is the activation energy for the conductivity relaxation and τ_0 is the free exponential factor. The activation energy is estimated from the measured slope of $\ln\tau$ versus $1000/T$ and is found to be 0.075 eV.

Figure 8c shows the Nyquist plot (Z' versus Z'') of the Cu/InTeSe/Cu structure measured at different temperatures that exhibits the presence of single semicircle arcs. The decrease in radius of the semicircular arcs with increase in temperature indicates the mechanism of temperature-dependent relaxation process. Appearance of dominant single semicircular arcs in the plots could be due to the grain effect on the grain boundary and electrode effect of the investigated material [50, 51]. Furthermore, the temperature-dependence grain and grain boundary resistance (R) for the present system have been investigated. The resistance is found to decrease with increase in temperature from the intercept of the semicircular arcs on Z' values. The evaluated Z' values are presented in Table 5. This impedance spectrum can be modeled as an equivalent [50] circuit, which consists of a parallel combination of bulk resistance and capacitance.

Complex impedance spectroscopy is used to describe the electrical behavior of $\text{In}_2(\text{Te}_{1-x}\text{Se}_x)_3$ thin film in the present work. Grain and grain boundary contributions to the electrical properties (dielectric constant, conductivity) of dielectric materials can be determined using the differences in their responses to the applied field by equivalent circuit (as shown in Fig. 9). The equivalent circuit model consists of parallel resistor–capacitor elements connected in series [52]. Here, the circuit is composed of an array of two subcircuits in series, the low-frequency response corresponds to grain boundary response (R_{gb}) and the high-frequency response corresponds to grain response (R_g). Nyquist plot exhibits the appearance of depressed semicircle with the center lying on the straight line below the real axis. Therefore, the equivalent circuit is replaced by constant phase element instead of capacitor. The equivalent circuit fitting parameter is obtained using Z-View software. Theoretical values of grain boundary resistance and bulk resistance were investigated from the intercept of the semicircular arcs. The following relation was used to determine the capacitances,

$$\omega_{\max}RC = 1,$$

where ω_{\max} is the angular frequency at the maxima of the semicircle.

Table 5 Variation of the resistance of In–Te–Se nanocomposite thin film with temperature

Temperature (K)	100	150	200	250	300
Resistance (kΩ)	66.55	33.60	17.56	14.02	5.24

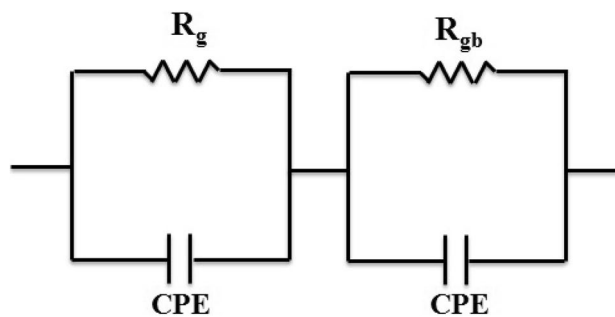


Fig. 9 Equivalent circuit used to represent the electrical properties of $\text{In}_2(\text{Te}_{1-x}\text{Se}_x)_3$ thin film

3.6 Optical analysis

Generally, optical studies are very important to understand the effect of doping of additional elements. In addition to that, it can be used to evaluate the band structure and band gap energy of the material. Figure 10 shows the transmittance versus wavelength spectra and the Tau's plot of $\text{In}_2(\text{Te}_{1-x}\text{Se}_x)_3$ thin films. The appearance of minimum and maximum intensity peaks denote the optical interference pattern, confirming the formation of layered structure in the prepared sample. From the Tau's plot, the band gap energy is found to be 1.10 eV. The band gap energy of In_2Te_3 is about 1.35 eV and that of In_2Te_3 is 1.01 [53]. Thus, this confirms the doping of Se in the In_2Te_3 phase and also the values are comparable to the earlier reports. [53]. It also shows that the addition of a third element could also lead to tailoring of the band gap energy of the system to be utilized in photovoltaic devices. Doping additional elements in the ternary compounds modifies the optical and electrical properties.

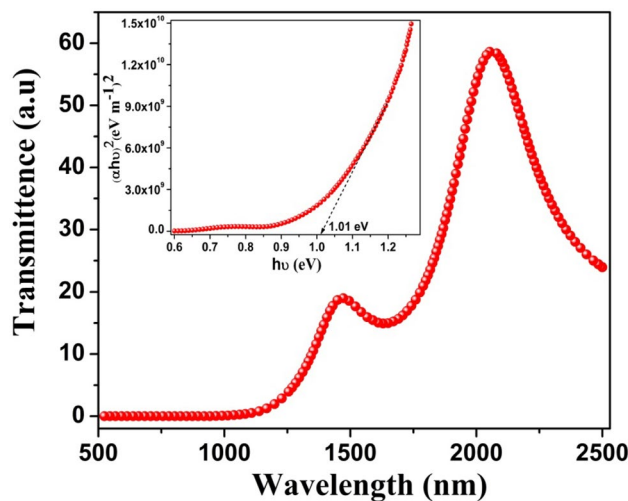


Fig. 10 The optical transmittance spectrum and Tau's plot of In–Se–Te nanocomposites thin films

As reported above, the optical band gap changes to 1.10 eV compared to end members band gaps of 1.01 eV (In_2Te_3) and 1.35 eV (In_2Se_3). Additionally, the electrical properties are also modified due to doping of Se.

4 Conclusion

AC conductivity and dielectric properties of thermally evaporated Cu/InTeSe/Cu structure were studied in the frequency range 20 kHz to 2 MHz at 100–300 K. The addition of Se into In–Te chalcogenide enhances the AC conductivity and dielectric properties as a function of frequency and temperature. In the present ternary $\text{In}_2(\text{Te}_{1-x}\text{Se}_x)_3$ system, larger dielectric constant values ~ 17 at 300 K were achieved at 303 K. The temperature- and frequency-dependent ϵ' , $\tan\delta$, and σ_{ac} were measured; the values of C and ϵ' decreased with frequency, while σ_{ac} increased with both temperature and frequency. The mechanism responsible for AC conduction is due to electronic hopping. Nyquist plot exhibits both bulk and grain boundary response and also reveals that grain and grain boundary resistance decrease with the increase in temperature. The decrease in radius of the semicircular arcs with increase in temperature denotes the mechanism of the temperature-dependent relaxation process. The impedance spectrum of $\text{In}_2(\text{Te}_{1-x}\text{Se}_x)_3$ can be modeled as an equivalent circuit which consists of a parallel combination of bulk resistance and capacitance.

Acknowledgements The author greatly acknowledges the Inter University Accelerator Centre (IUAC) New Delhi, for providing financial support through the project UFUP-57306.

References

- Z. Zheng, J. Yao, G. Yang, A.C.S. Appl. Mater. Interfaces **9**, 7288–7296 (2017). <https://doi.org/10.1021/acsami.6b16323>
- J.O. Island, S.I. Blanter, M. Buscema, H.S.J. Van Der Zant, A. Castellanos-Gomez, Nano Lett. **15**, 7853–7858 (2015). <https://doi.org/10.1021/acs.nanolett.5b02523>
- W. Feng, W. Zheng, X. Chen, G. Liu, W. Cao, P. Hu, Chem. Mater. **27**, 983–989 (2015). <https://doi.org/10.1021/cm504268j>
- H. Lee, Y.K. Kim, D. Kim, D.H. Kang, IEEE Trans. Magn. **41**, 1034–1036 (2005). <https://doi.org/10.1109/TMAG.2004.842032>
- A. Politano, D. Campi, M. Cattelan, I. Ben Amara, S. Jaziri, A. Mazzotti, A. Barinov, B. Gürbulak, S. Duman, S. Agnoli, L.S. Caputi, G. Granozzi, A. Cupolillo, Sci. Rep. **7**, 1–11 (2017). <https://doi.org/10.1038/s41598-017-03186-x>
- P. Nayebi, M. Emami-razavi, E. Zaminpayma, J. Phys. Chem. **120**, 4589–4595 (2016). <https://doi.org/10.1021/acs.jpcc.5b10749>
- M.M. El-Nahass, A.A. Attia, G.F. Salem, H.A.M. Ali, M.I. Ismail, Phys. B **434**, 89–94 (2014). <https://doi.org/10.1016/j.physb.2013.10.049>
- A. Sharma, N. Mehta, RSC Adv. **7**, 19085 (2017). <https://doi.org/10.1039/c7ra00010c>
- N. Shukla, D.K. Dwivedi, J. Asian Ceram. Soc. **4**, 178–184 (2016). <https://doi.org/10.1016/j.jascr.2016.02.003>
- C. Dohare, M.M.A. Imran, N. Mehta, J. Asian Ceram. Soc. **4**, 252–258 (2016). <https://doi.org/10.1016/j.jascr.2016.04.003>
- E. Abd El-Wahabb, A.M. Farid, A.M. Shakra, Appl. Phys. A. **124**, 666 (2018). <https://doi.org/10.1007/s00339-018-2098-z>
- N. Sharma, B.S. Patial, N. Thakur, Appl. Phys. A **122**, 209 (2016). <https://doi.org/10.1007/s00339-016-9728-0>
- N.F. Mott, *Conduction in non-crystalline materials*, 2nd edn. (Clarendon Press, Oxford, 1993)
- A.S. Hassanien, J. Alloys Compd. **671**, 566–578 (2016). <https://doi.org/10.1016/j.jallcom.2016.02.126>
- S.S. Fouad, H.E. Atyia, J. Alloys Compd. **688**, 1206–1213 (2016). <https://doi.org/10.1016/j.jallcom.2016.07.091>
- J. Sharma, S. Kumar, Turk. J. Phys. **35**, 349–358 (2011). <https://doi.org/10.3906/fiz-1003-9>
- J. Sharma, S. Kumar, Glob. J. Sci. Front. Res. Phys. Space Sci. **13**, 1 (2013)
- H. Kumar, A. Sharma, N. Mehta, Mater. Lett. **121**, 194–197 (2014). <https://doi.org/10.1016/j.matlet.2014.01.146>
- N. Chandel, N. Mehta, A. Kumar, Solid State Sci. **13**, 257–262 (2011). <https://doi.org/10.1016/j.solidstatesciences.2010.11.025>
- N. Chandel, N. Mehta, A. Kumar, Curr. Appl. Phys. **12**, 405–412 (2012). <https://doi.org/10.1016/j.cap.2011.07.038>
- C. Dohare, N. Mehta, A. Kumar, Mater. Chem. Phys. **127**, 208–213 (2011). <https://doi.org/10.1016/j.matchemphys.2011.01.067>
- B.S. Patial, N. Neha, S.K. Thakur, Tripathi. Int. J. Adv. Res. Phys. Sci. **1**, 9–16 (2014)
- M. Pandian, P. Matheswaran, B. Gokul, R. Sathyamoorthy, R. Meena, K. Asokan, AIP Adv. **8**, 115015 (2018). <https://doi.org/10.1063/1.5057734>
- M. Pandian, P. Matheswaran, B. Gokul, R. Sathyamoorthy, K. Asokan, Appl. Surf. Sci. **449**, 55–67 (2018). <https://doi.org/10.1016/j.apsusc.2018.01.027>
- P. Matheswaran, R. Sathyamoorthy, R. Saravanakumar, S. Velumani, Mater. Sci. Eng. B. **174**, 269–272 (2010). <https://doi.org/10.1016/j.mseb.2010.03.008>
- N. Shiwakoti, A. Bobby, K. Asokan, B. Antony, Mater. Sci. Semicond. Process. **42**, 378–382 (2016). <https://doi.org/10.1016/j.mssp.2015.11.010>
- A. Tataroglu, S. Altindal, M.M. Bulbul, Microelectron. Eng. **81**, 140–149 (2005). <https://doi.org/10.1016/j.mee.2005.04.008>
- R. Padma, B.P. Lakshmi, V.R. Reddy, Superlattices Microstruct. **60**, 358 (2013). <https://doi.org/10.1016/j.spmi.2013.05.014>
- C.J. Ridge, P.J. Harrop, D.S. Campbell, Thin Solid Films **2**, 413–422 (1968). [https://doi.org/10.1016/0040-6090\(68\)90055-2](https://doi.org/10.1016/0040-6090(68)90055-2)
- T.I. Koba, T. Wagner, P.J.S. Ewen, A.E. Owen, Philos. Mag. B **71**, 311–318 (1995). <https://doi.org/10.1080/13642819508239036>
- C.G. Koops, Phys. Rev. **83**, 121–124 (1951). <https://doi.org/10.1103/PhysRev.83.121>
- F. Argall, A.K. Jonscher, Thin Solid Films (1968). [https://doi.org/10.1016/0040-6090\(68\)90002-3](https://doi.org/10.1016/0040-6090(68)90002-3)
- H.M. Zeyada, M.M. Makhlof, Appl. Phys. A **119**, 1109–1118 (2015). <https://doi.org/10.1007/s00339-015-9076-5>
- H.M. Zeyada, M.M. El-Nahass, M.M. Makhlof, Curr. Appl. Phys. **11**, 1326–1331 (2011). <https://doi.org/10.1016/j.cap.2011.03.074>
- H. Birey, Dielectric properties of aluminum oxide films. J. Appl. Phys. **49**, 2898 (1978). <https://doi.org/10.1063/1.325174>
- Y. Şafak-Asar, T. Asar, Ş. Altindal, S. Özgelik, J. Alloys Compd. **628**, 442–449 (2014). <https://doi.org/10.1016/j.jallcom.2014.12.170>
- J.M. Stevels, in *Electrical Conductivity II/Elektrische Leitungsphänomene II. Handbuch der Physik/Encyclopedia of Physics*, vol. 20 (Springer, Berlin, 1997), p. 350. https://doi.org/10.1007/978-3-642-45859-0_3
- A.M. Farid, H.E. Atyia, N.A. Hegab, Vacuum **80**, 284 (2005). <https://doi.org/10.1016/j.vacuum.2005.05.003>

39. M. Ram, S. Chakrabarti, J. Alloys Compd. **462**, 214–219 (2008). <https://doi.org/10.1016/j.jallcom.2007.08.001>
40. E.B. Fleisher, C.K. Miller, L.R. Webb, J. Am. Soc. **86**, 2342 (1964)
41. M.M. El-Nahass, H.M. Zeyada, E.M. El-Menyay, Eur. Phys. J. Appl. Phys. **48**, 10301 (2010)
42. Anjali, B.S. Patial, S. Bhardwaj, A.M. Awasthi, N. Thakur, Phys. B. **523**, 52–61 (2017). <https://doi.org/10.1016/j.physb.2017.08.001>
43. K.M. Diederichsen, H.G. Buss, B.D. McCloskey, Macromolecules **50**, 3831–3840 (2017). <https://doi.org/10.1021/acs.macromol.7b00423>
44. S. Breuer, M. Wilkening, Dalton Trans. **47**, 4105–4117 (2018). <https://doi.org/10.1039/C7DT04487A>
45. N. Mehta, A. Kumar, J. Phys. Chem. B **120**, 1175–1182 (2016). <https://doi.org/10.1021/acs.jpcc.5b10441>
46. G. Mohsin, M. Zulfeqar, Acta Phys. Pol. A **128**, 59–63 (2015). <https://doi.org/10.12693/APhysPola.128.59>
47. N.A. Hegab, M.A. Afifi, H.E. Atyia, M.I. Ismael, Acta Phys. Pol. A **119**, 416 (2011). <https://doi.org/10.12693/aphyspola.119.416>
48. I.S. Yahia, N.A. Hegab, A.M. Shakra, A.M. Al-Ribaty, Phys. B. **407**, 2476–2485 (2012). <https://doi.org/10.1016/j.physb.2012.03.049>
49. P.S. Sahoo, A. Panigrahi, S.K. Patri, R.N.P. Choudhary, Mater. Sci. Pol. **28**, 763 (2010). <https://doi.org/10.1016/j.physb.2014.06.036>
50. R. Das, T. Sarkar, K. Mandal, J. Phys. D Appl. Phys. **45**, 455002 (2012). <https://doi.org/10.1088/0022-3727/45/45/455002>
51. B.P. Das, R.N.P. Choudhary, P.K. Mahapatra, Indian J. Eng. Mater. Sci. **15**, 152 (2008)
52. J. Liu, C. Duan, W.N. Mei, R.W. Smith, J.R. Hardy, J. Appl. Phys. **98**, 093703 (2005). <https://doi.org/10.1063/1.2125117>
53. S. Sen, D.N. Bose, Solid State Commun. **50**, 39–42 (1984). [https://doi.org/10.1016/0038-1098\(84\)90055-3](https://doi.org/10.1016/0038-1098(84)90055-3)

Publisher's Note Springer Nature remains neutral with regard to jurisdictional claims in published maps and institutional affiliations.